AGU PUBLICATIONS

Geophysical Research Letters

RESEARCH LETTER
10.1002/2013GL058918

Key Points:
- Global receiver function stacks revealed mantle stratification
- A positive 300 km and a negative 600 km discontinuity are observed
- Slant-stack technique identifies the primary conversions from the multiples

Supporting Information:
- Readme
- Figures S1–S3

Correspondence to:
X. Yuan,
yuan@gfz-potsdam.de

Citation:
Shen, X., X. Yuan, and X. Li (2014), A ubiquitous low-velocity layer at the base of the mantle transition zone, *Geophys. Res. Lett.*, *41*, 836–842, doi:10.1002/2013GL058918.

Received 1 DEC 2013
Accepted 15 JAN 2014
Accepted article online 17 JAN 2014
Published online 11 FEB 2014

A ubiquitous low-velocity layer at the base of the mantle transition zone

Xuzhang Shen[1], Xiaohui Yuan[2], and Xueqing Li[2]

[1]Lanzhou Institute of Seismology, China Earthquake Administration, Lanzhou, China, [2]Deutsches GeoForschungsZentrum GFZ, Potsdam, Germany

Abstract Global stacks of receiver functions clearly exhibit the upper mantle stratification. Besides the most prominent seismic discontinuities, such as the Moho and the 410 and 660 km discontinuities, a negative discontinuity is detected at a depth of ~600 km, indicating a low-velocity layer at the base of the mantle transition zone. The slant-slack technique helps to identify the primary conversions from the multiple reverberations. Presence of the negative 600 km discontinuity underneath both continent and ocean island stations, where the crustal thickness significantly differs, also precludes the possible cause of crustal reverberations. We conclude that the negative 600 km discontinuity could be a global feature, possibly resulted from accumulation of ancient subducted oceanic crust. The X-discontinuity at ~300 km depth is also observed in our global stacks, which can be explained by the coesite-stishovite phase transformation.

1. Introduction

Seismic discontinuities in the Earth's mantle are commonly regarded as phase transformations of the mantle mineral constituents, such as olivine, pyroxene, and garnet [*Jeanloz and Thompson*, 1983]. The most prominent mantle discontinuities are the 410 and 660 km discontinuities (referred to as the 410 and the 660, respectively), which define the mantle transition zone (MTZ) separating the upper and lower mantle [*Helffrich*, 2000]. The 410 and 660 are mainly considered as mineral phase transformations of olivine into high-pressure forms, which create sharp vertical gradients in density and seismic velocity. The 410 marks the transition from olivine to wadsleyite, and the 660 marks the transition from ringwoodite to perovskite + magnesiowüstite. The transition from wadsleyite to ringwoodite (the 520 km discontinuity) is probably a gradient phase change and may occur at varying depth levels [*Shearer*, 1990; *Deuss and Woodhouse*, 2001]. In some regions, phase transformations of minor mantle constituents, such as garnet, become significant and cause additional discontinuities and complication in the MTZ structures [*Vacher et al.*, 1998]. Other discontinuities at different depths are frequently observed, including, e.g., the Lehmann discontinuity at ~220 km depth [*Gu et al.*, 2001; *Deuss and Woodhouse*, 2002], the X-discontinuity at ~300 km depth [*Deuss and Woodhouse*, 2002; *Bagley and Revenaugh*, 2008; *Schmerr et al.*, 2013; *Ramesh et al.*, 2005].

Seismic discontinuities can generate mode conversions of seismic body waves and therefore can be visualized by looking at converted seismic waves. The receiver function analysis is a well-established method for detecting *P*-to-*S* converted phases below seismic stations. The method is applicable mostly for continents and ocean islands where seismic stations can be deployed. Previous studies verified the global existence of the 410 and 660 [*Stammler et al.*, 1992; *Li et al.*, 2003; *Lawrence and Shearer*, 2006]. Here we stack ~30,000 receiver functions of 169 globally distributed seismic stations, which clearly exhibit stratification of the upper mantle. In addition to the most prominent MTZ discontinuities (the 410 and 660), we observed two other discontinuities with different signs at depths of ~300 and ~600 km, respectively. The former is often called the X-discontinuity and is previously observed in diverse regions [*Deuss and Woodhouse*, 2002; *Bagley and Revenaugh*, 2008; *Schmerr et al.*, 2013; *Ramesh et al.*, 2005]. The latter is less known and is only sporadically observed [*Shen and Blum*, 2003; *Shen et al.*, 2008; *Jasbinsek and Dueker*, 2007; *Eagar et al.*, 2010; *Bonatto et al.*, 2013].

In this paper we use the notations of Pds and PPds for the primary *P*-to-*S* conversion and the first multiple, respectively, where d denotes the depth of the discontinuity.

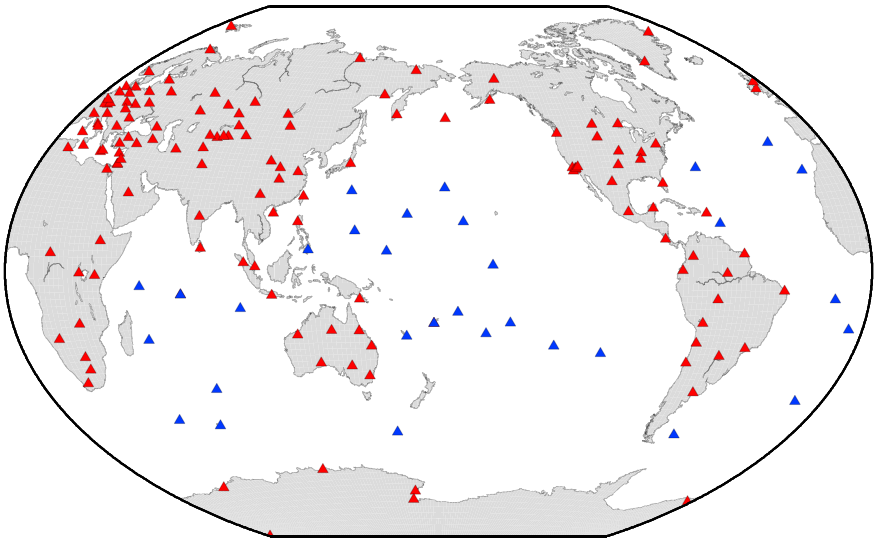

Figure 1. Location of global seismic stations used in this study. Red and blue triangles denote the continent and ocean stations, respectively.

2. Data and Method

Figure 1 shows the distribution of the 169 permanent seismic stations used in this study. Of these stations, 139 are located in continents (continent stations), while 30 on ocean islands (ocean stations). Waveform data for teleseismic events at epicentral distances of 30–95° and with magnitudes larger than 5.7 are requested from the Incorporated Research Institutions for Seismology (IRIS) and GEOFON data centers. The receiver function calculation mainly includes a coordinate rotation from the Z-N-E system to the ray-based L-Q-T coordinate system and a deconvolution of the L component from the Q component for each event [*Yuan et al*., 1997]. The L, Q, and T components correspond to the P, SV, and SH polarization directions, respectively. The new coordinate system is determined by diagonalization of the covariance matrix [*Montalbetti and Kanasewich*, 1970], which minimizes the Q and T amplitudes at the *P* arrival. The deconvolution is performed in time domain by a Wiener filtering approach [*Berkhout*, 1977]. Receiver functions are generated by convolution of L,Q,T component waveforms with an inverse filter that was obtained by minimizing the least square difference between the L component and a desired delta-like spike function within an 80 s time window. As we are interested in the global average mantle structure, only the Q component receiver functions are considered in this study. All the observed receiver functions are divided into two groups according to station locations, either in continents or in oceans. For each group we sorted the receiver functions by epicentral distances and constructed binning stacks of receiver functions in a distance interval of 0.5° (Figures 2a and 2b). A low-pass filter of 5 s was applied before stacking. Although the number of original receiver functions used for the ocean stacks (~2700) are significantly less than that for the continent stacks (~27,000), the major converted phases can be identified in both sections. Strong interfering PP and PcP phases are present in the continent stacks, while they are weaker in the ocean stacks. This difference may be explained by the coordinate rotation, where theoretical incidence angles based on the IASP91 model [*Kennett and Engdahl*, 1991] are used. Missing thick sediment layers beneath most of the ocean stations allows for a more optimal rotation with less projection of *P* wave amplitudes on the Q components. Another distinct difference is the duration of the crustal phases. In the continent stacks the primary conversions and the crustal multiples dominate the first 30 s, whereas they are within the first 10 s in the ocean stacks.

3. Observations

Both the continent and ocean stacks (Figures 2a and 2b) exhibit clear *P*-to-*S* converted signals of the 410 (P410s) and 660 (P660s). Their arrival times in the continent section agree with those predicted by the IASP91 model. In the ocean section both phases arrive simultaneously ~5 s later due to slower upper mantle beneath oceans seen by seismic tomography [*Grand*, 1994]. The multiple of the 410 (PP410s) are well recognized with different slowness at 130–140 s. The Lehmann discontinuity at 220 km depth and the 520 km discontinuity

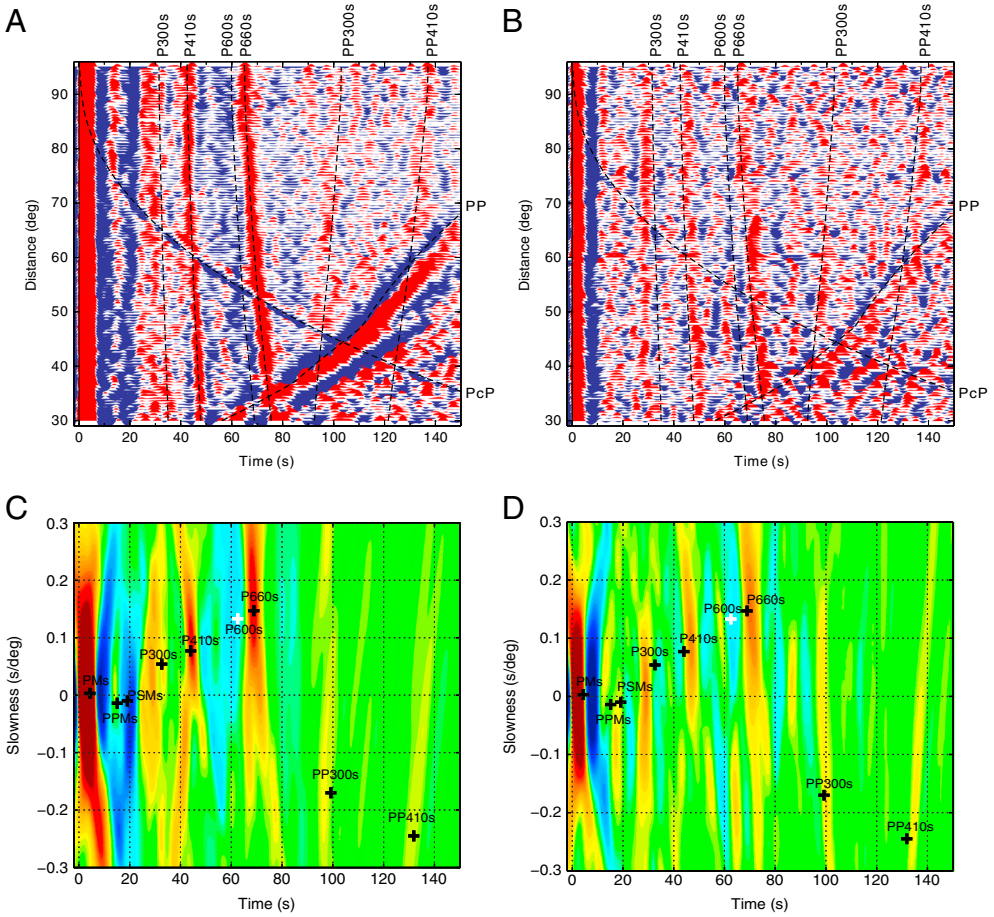

Figure 2. Stacks of receiver functions of (a) continent and (b) ocean stations in bins of epicentral distance of 0.5°. All receiver functions are filtered with a band-pass Butterworth filter of 5–50 s. Positive and negative amplitudes are shaded in red and blue, respectively. Black dashed lines are reference arrival times of the P300s, P410s, P600s, P660s, PP300s, PP410s as well as of the PP and PcP, predicted by the IASP91 model. Slant stacks of (c) continent and (d) ocean receiver functions as a function of slowness. Red and blue colors denote positive and negative amplitudes, respectively. The slowness values are relative to the incident *P* phase. Primary converted phases and multiple reverberations are thus separated into positive and negative slowness ranges, respectively. The theoretical locations of the P300s, P410s, P660s, PP300s, and PP410s phases are marked by black pluses. The white cross denotes the P600s phase.

are not coherently observed, suggesting that either they do not exist globally or they subject to large depth variability. In the ocean stacks (Figure 2b) a pronounced negative converted phase appears at ~9 s, probably representing the oceanic lithosphere-asthenosphere boundary (LAB) with an average depth of ~80 km. The first 30 s of the continent stacks is overwhelmed by the crustal reverberations, which mask the continental LAB phase. In 25–30 s a positive converter seems visible, likely representing the X-discontinuity (P300s). The phase seems to be clearer in the ocean section, whereas it is contaminated by the crustal multiples in the continent section. However, the phase in the ocean section has a slowness close to zero, making it a little ambiguous as a clear detector of the X-discontinuity. Interference of reverberations in the shallower layers may explain the slowness deviation. More solid evidence for the X-discontinuity is made by the topside reflections (PP300s). In both sections a positive phase between 90 and 100 s is well recognizable, which could represent the multiple reverberation of the X-discontinuity.

A negative converted phase is clearly visible between 60 and 70 s leading the P660s. The phase is parallel to the P660s and arrives earlier than the P660s by 6–8 s, indicating a discontinuity at a depth of ~600 km with reduced seismic velocities below it. The phase arrives at similar times in the continent and ocean sections, although the crustal thickness is distinctly different in these two regions. Therefore, this phase cannot be caused by crustal multiples. We interpret this phase as a 600 km discontinuity with negative impedance contrast, which possibly exist globally.

Table 1. Amplitudes of Observed Pds Phases and the Shear Wave Velocity (Vs) Jumps of the Mantle Discontinuities[a]

Discontinuity Depth (km)	Pds Amplitude (Continent)	Vs Jump (Continent) (%)	Pds Amplitude (Ocean)	Vs Jump (Ocean) (%)	Pds Amplitude (IASP91)	Vs Jump (IASP91) (%)
300	0.009 ± 0.001	2.2 ± 0.2	0.027 ± 0.006	4.8 ± 1.1	—	—
410	0.018 ± 0.001	4.4 ± 0.2	0.032 ± 0.007	5.7 ± 1.2	0.025	4.1
600	−0.009 ± 0.001	−2.2 ± 0.2	−0.022 ± 0.009	−3.9 ± 1.6	—	—
660	0.025 ± 0.001	6.2 (fixed)	0.035 ± 0.008	6.2 (fixed)	0.044	6.2

[a]The Vs jumps are relatively adjusted to that of the 660, which is fixed to 6.2% according to the IASP91 model. Errors in the amplitude measurements are given by standard deviations of 100 bootstrap estimates, each randomly sampling a subset of 60% of entire data.

We slant-stacked receiver functions as a function of time and slowness (Figures 2c and 2d). The slant-stack technique [*Schultz and Claerbout*, 1978] can determine the slowness of the converted phases, thus separating the primary conversions from the multiples. The maxima in the positive slowness range represent the primary conversions, whereas the multiples appear in the negative slowness range. In Figures 2c and 2d we can see the converted phases of the positive Moho, X-discontinuity, the 410 and 660, as well as the negative 600 km discontinuity. The multiples of the Moho, the X-discontinuity, and the 410 are visible in the negative slowness range. Their phase slownesses are close to the theoretical expectations. The slant stack confirms the observation of the 600 km discontinuity by the direct *P*-to-*S* converted wave instead of multiples from shallower depths. At time around 60 s the P600s is well separated by some multiple energy that appears in the negative slowness range. The X-discontinuity is more reliably observed by the PP300s phase.

The discontinuities at 300 and 600 km depths can be consistently observed in different frequency bands (Figures S1 and S2). They can be sharply identified in broadband data (Figure S1) and become more coherent in longer periods (Figure S2). Figure S3 shows slant stacks of subsets of receiver functions grouped in different continents. More than 3000 receiver functions are stacked for Europe, Asia (including Australia), and North America, whereas less data are available for South America and Africa, making these stacks noisier and less reliable. Nevertheless, the negative 600 km discontinuity seems to be visible in nearly all continents. The X-discontinuity is less consistent. It is strong in North America, visible in Europe, but weak in Asia.

Amplitudes of the mantle-converted phases can be used to determine shear wave velocity contrasts of the discontinuities. We stacked all individual receiver functions after moveout correction for the primary conversion and measured the amplitudes of the mantle Pds phases (Table 1). The measurement was separately done for continent and ocean stacks. We also calculated the Pds amplitudes for the 410 and 660 in the IASP91 model. The absolute amplitudes in the global stacks may be suppressed by diverse factors, such as scattering caused by the 3-D Earth heterogeneity, topography and sharpness of the discontinuities, and poor data quality. Stacking heterogeneous data may underestimate the velocity jump of the discontinuity. Therefore, we measure relative amplitudes among different discontinuity phases. We fixed the velocity jump of the 660 to the IASP91 model (6.2%) and calculated the velocity jumps of other discontinuities. The estimated velocity jump of the 410 (4.4%) is very close to that of the IASP91 model (4.1%) for the continent, whereas it is higher (5.7%) for the ocean. The number of receiver functions for the continent stack is 10 times more than that for the ocean stack. Therefore, the amplitudes in the continent stack are considered more reliable than those in the ocean stack. The velocity jumps of the 300 and the 600 are 2.2% and −2.2%, respectively. Errors in the velocity jumps estimated by the bootstrap method are very small for continents due to the large amount of data used, whereas they are much bigger for oceans.

We calculate synthetic receiver functions for two different models. The first model is based on the IASP91 model, simplified to contain one gradient crust layer (Figure 3a). In the second model we added a positive discontinuity at a depth of 300 km and a negative done at a depth of 600 km (Figure 3b). Full-wavefield synthetic seismograms were generated using the reflectivity method [*Kind*, 1976]. Synthetic receiver functions were then calculated following similar processing steps as for the observed waveforms. The binning stack sections (Figures 3c and 3d) show similar features as those of the observed data. Due to the use of a homogeneous 1-D model and low noise level, some multiples of higher orders are also visible. They are, however, dramatically attenuated in the observed data by the Earth heterogeneity along the raypaths. The synthetic receiver functions for the model with the positive 300 km and the negative 600 km discontinuities are well consistent with the observed receiver functions. The slant slacks (Figures 3e and 3f) clearly show that both the positive 300 km and the negative 600 km discontinuity are required to explain the observation.

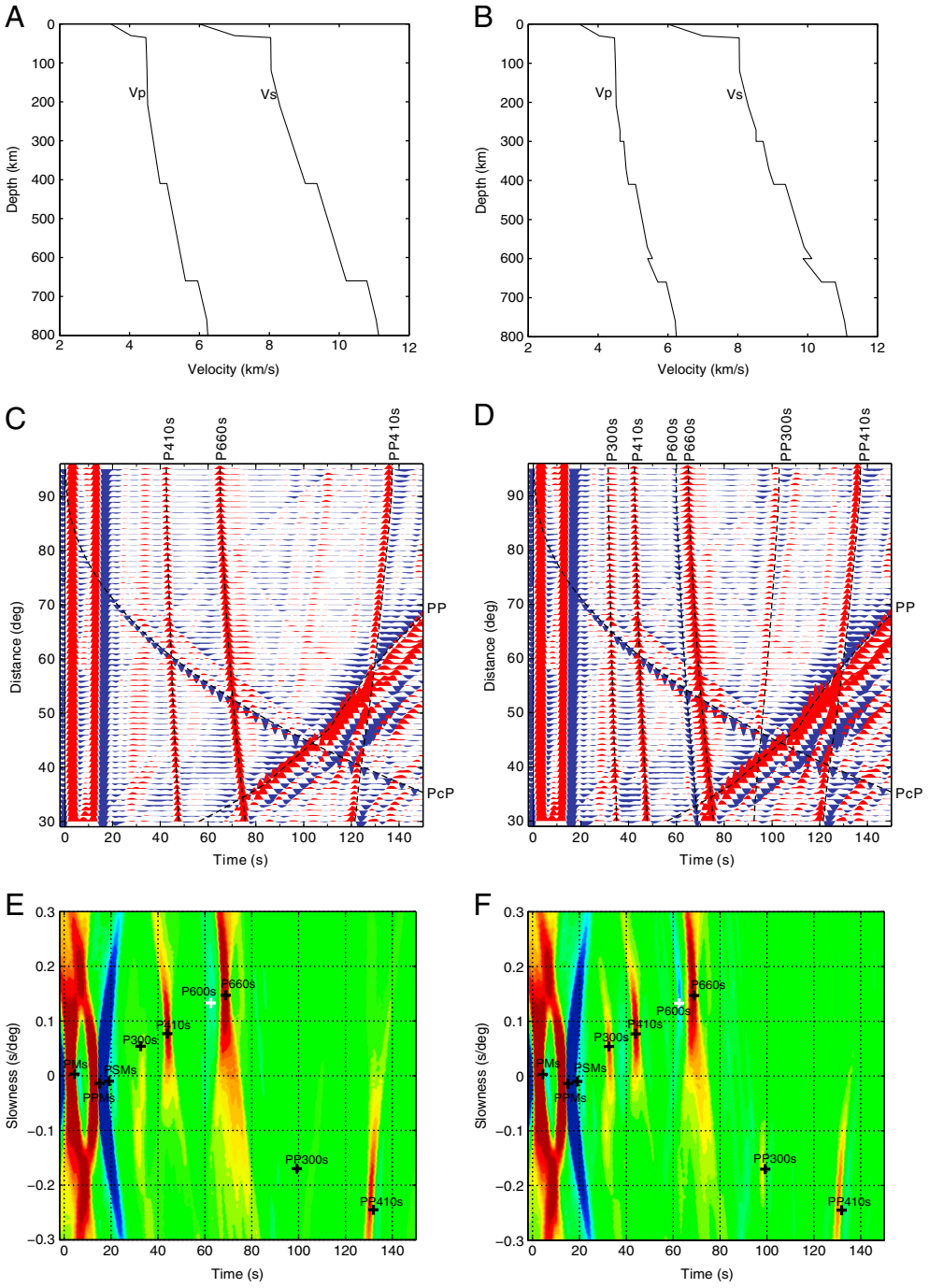

Figure 3. One-dimensional velocity model modified from the IASP91 model (a) with one gradient crustal layer and (b) with a positive and a negative discontinuity at 300 and 600 km, respectively. (c and d) Synthetic receiver functions for the model in Figure 3a and 3b. Positive and negative amplitudes are shaded in red and blue, respectively. Reference phases for the IASP91 model from Figure 2a are plotted and labeled. (e and f) Slant stacks of the synthetic receiver functions of Figure 3c and 3d. Theoretical locations of some reference phases are indicated.

4. Discussions

The negative 600 km discontinuity within the MTZ have been previously observed at different depths beneath South Africa [*Shen and Blum*, 2003], China [*Shen et al*., 2008], North America [*Jasbinsek and Dueker*, 2007; *Eagar et al*., 2010], and Iberia [*Bonatto et al*., 2013]. The shear wave velocity reduction associated with the 600 km discontinuity was estimated to be 2.2% by *Shen and Blum* [2003] and 7.4% by *Jasbinsek and Dueker*

[2007]. The low-velocity layer at the base of the MTZ was considered as a local phenomenon and was explained by accumulation of ancient subducted oceanic crust [*Shen and Blum*, 2003]. Our observation of the 600 km discontinuity in receiver function stacks with globally distributed seismic stations suggests that it can be a global feature. The velocity jump of the 600 is 2.2%, same as that beneath South Africa, estimated by *Shen and Blum* [2003].

Accumulation of oceanic crust in the mantle transition zone is a global phenomenon. Phase transformations occurred within the subducted oceanic crust make its density favorable to allow it accumulating at the base of the MTZ [*Ringwood*, 1969; *Irifune and Ringwood*, 1993; *Shen and Blum*, 2003]. Stagnant slabs, which are widely recognized in most subduction zones by seismic tomography [*Fukao et al*., 2009], bring significant oceanic crust into the MTZ. Numerical modeling shows that accumulation of oceanic crustal by stagnant slabs can cause a high-velocity zone in the mid-MTZ, hence creating a low-velocity zone below [*Zhang et al*., 2013]. Significant amount of water can be transported with the subduction of hydrous oceanic crust to the MTZ. Excess water content could reduce seismic velocities at the base of the MTZ [*Inoue et al*., 1998], which may generate the negative 600. Based on the assumption that the existence of the 600 is a local phenomenon, *Shen and Blum* [2003] argued that the increased water content should also increase the 660 velocity jump, which was not observed beneath South Africa, where the negative 600 was observed. However, if the 600 is a global feature, the excess water at the base of the MTZ, if it exists, should have already contributed to the global average velocity jump of the 660. Additionally, a sound velocity measurement of majorite garnet, a significant high-pressure phase in the MTZ, showed that it may cause substantial low shear wave velocity in the lower part of the MTZ [*Irifune et al*., 2008].

The X-discontinuity has been previously observed in many regions with a variety of tectonic settings [*Deuss and Woodhouse*, 2002; *Bagley and Revenaugh*, 2008; *Schmerr et al*., 2013; *Ramesh et al*., 2005]. Out of a number of mechanisms that have been proposed to create the X-discontinuity [*Schmerr et al*., 2013; *Williams and Revenaugh*, 2005], the mineral phase transformation of coesite to stishovite in an eclogite-rich mantle composition is thought to be the most plausible explanation [*Williams and Revenaugh*, 2005; *Liu et al*., 1996]. The *P* and *S* wave velocities in stishovite are $>$30% higher than those of the coesite; thus, a small percentage of free silica (4–10%) is sufficient to generate the X-discontinuity [*Williams and Revenaugh*, 2005]. Here we observed a Vs jump of 2.2%, which can be explained by 9% free silica content in the upper mantle.

Acknowledgments

The work was funded by the Deutsche Forschungsgemeinschaft and the National Natural Science Foundation of China (grant 41274093). Waveform data were provided by the IRIS and GEOFON data centers. We thank Hitoshi Kawakatsu for helpful discussion. The Seismic Handler [*Stammler*, 1993] was used in the data processing and the GMT [*Wessel and Smith*, 1998] for plotting. Comments of two anonymous reviewers helped to improve the manuscript.

The Editor thanks two anonymous reviewers for their assistance in evaluating this paper.

References

Bagley, B., and J. Revenaugh (2008), Upper mantle seismic shear discontinuities of the Pacific, *J. Geophys. Res.*, *113*, B12301, doi:10.1029/2008JB005692.

Berkhout, A. J. (1977), Least-squares inverse filtering and wavelet deconvolution, *Geophysics*, *42*, 1369–1383.

Bonatto, L., M. Schimmel, J. Gallart, and J. Morales (2013), Studying the 410-km and 660-km discontinuities beneath Spain and Morocco through detection of P-to-S conversions, *Geophys. J. Int.*, *194*, 920–935, doi:10.1093/gji/ggt129.

Deuss, A., and J. H. Woodhouse (2001), Seismic observations of splitting of the mid-transition zone discontinuity in Earth's mantle, *Science*, *294*, 354–357.

Deuss, A., and J. H. Woodhouse (2002), A systematic search for mantle discontinuities using SS-precursors, *Geophys. Res. Lett.*, *29*(8), 901–904, doi:10.1029/2002GL014768.

Eagar, K. C., M. J. Fouch, and D. E. James (2010), Receiver function imaging of upper mantle complexity beneath the Pacific Northwest, United States, *Earth Planet. Sci. Lett.*, *297*, 141–153.

Fukao, Y., M. Obayashi, T. Nakakuki, and the Deep Slab Project Group (2009), Stagnant slab: A review, *Annu. Rev. Earth Planet. Sci.*, *37*, 19–46.

Grand, S. P. (1994), Mantle shear structure beneath the Americas and surrounding oceans, *J. Geophys. Res.*, *99*, 11,591–11,621.

Gu, Y., A. M. Dziewonski, and G. Ekstrom (2001), Preferential detection of the Lehmann discontinuity beneath continents, *Geophys. Res. Lett.*, *28*(24), 4655–4558.

Helffrich, G. (2000), Topography of the transition zone seismic discontinuity, *Rev. Geophys.*, *38*, 141–158.

Inoue, T., D. J. Weidner, P. A. Northrup, and J. B. Parise (1998), Elastic properties of hydrous ringwoodite (g-phase) in Mg2SiO4, *Earth Planet. Sci. Lett.*, *160*, 107–113.

Irifune, T., and A. E. Ringwood (1993), Phase transformation in subducted oceanic crust and buoyancy relationships at depths of 600-800 km in the mantle, *Earth Planet. Sci. Lett.*, *117*, 101–110.

Irifune, T., Y. Higo, T. Inoue, Y. Kono, H. Ohfuji, and K. Funakoshi (2008), Sound velocities of majorite garnet and the composition of the mantle transition region, *Science*, *451*, 814–817.

Jasbinsek, J., and K. Dueker (2007), Ubiquitous low-velocity layer atop the 410-km discontinuity in the northern Rocky Mountains, *Geochem. Geophys. Geosyst.*, *8*, Q10004, doi:10.1029/2007GC001661.

Jeanloz, R., and A. B. Thompson (1983), Phase transitions and mantle discontinuities, *Rev. Geophys.*, *21*, 51–74.

Kennett, B. L. N., and E. R. Engdahl (1991), Travel times for global earthquake location and phase identification, *Geophys. J. Int.*, *105*, 429–465.

Kind, R. (1976), Computation of reflection coefficients for layered media, *J. Geophys.*, *42*, 191–200.

Lawrence, J. F., and P. M. Shearer (2006), A global study of transition zone thickness using receiver functions, *J. Geophys. Res.*, *111*, B06307, doi:10.1029/2005JB003973.

Li, X., R. Kind, X. Yuan, S. V. Sobolev, W. Hanka, D. S. Ramesh, Y. Gu, and A. M. Dziewonski (2003), Seismic observation of narrow plumes in the oceanic upper mantle, *Geophys. Res. Lett.*, *30*(6), 1334, doi:10.1029/2002GL015411.

Liu, J., L. Topor, J. Zhang, A. Navrotsky, and R. C. Liebermann (1996), Calorimetric study of the coesite stishovite transformation and calculation of the phase boundary, *Phys. Chem. Min.*, *23*(1), 11–16.

Montalbetti, J. F., and E. R. Kanasewich (1970), Enhancement of teleseismic body phases with a polarization filter, *Geophys. J. Int.*, *21*, 119–129.

Ramesh, D. S., M. Ravi Kumar, E. Uma Devi, P. Solomon Raju, and X. Yuan (2005), Moho geometry and upper mantle images of northeast India, *Geophys. Res. Lett.*, *32*, L14301, doi:10.1029/2005GL022789.

Ringwood, A. E. (1969), Phase transformations in the mantle, *Earth Planet. Sci. Lett.*, *5*, 401–412.

Schmerr, N. C., B. M. Kelly, and M. S. Thorne (2013), Broadband array observations of the 300 km seismic discontinuity, *Geophys. Res. Lett.*, *40*, 841–846, doi:10.1002/grl.50257.

Schultz, P., and J. Claerbout (1978), Velocity estimation and downward-continuation by wavefront synthesis, *Geophysics*, *43*, 691–714.

Shearer, P. M. (1990), Seismic imaging of upper-mantle structure with new evidence for a 520-km discontinuity, *Nature*, *344*, 121–126.

Shen, X., H. Zhou, and H. Kawakatsu (2008), Mapping the upper mantle discontinuities beneath China with teleseismic receiver functions, *Earth Planet. Sci.*, *60*, 713–719.

Shen Y., and J. Blum (2003), Seismic evidence for accumulated oceanic crust above the 660-km discontinuity beneath southern Africa, *Geophys. Res. Lett.*, *30*(18), 1925, doi:10.1029/2003GL017991.

Stammler, K. (1993), SeismicHandler—Programmable multichannel data handler for interactive and automatic processing of seismological analysis, *Comp. Geosci.*, *19*, 135–140.

Stammler, K., R. Kind, N. Petersen, G. Kosarev, G. Vinnik, and Q. Liu (1992), The upper mantle discontinuities: Correlated or anticorrelated?, *Geophys. Res. Lett.*, *19*, 1563–1566.

Vacher, P., A. Mocquet, and C. Sotin (1998), Computations of seismic profiles from mineral physics: The importance of the non-olivine components for explaining the 660 km depth discontinuity, *Phys. Earth Planet. Inter.*, *106*, 275–298.

Wessel, P., and W. H. F. Smith (1998), New, improved version of the Generic Mapping Tool released, *EOS Trans. Am. Geophys. Union*, *79*, 579.

Williams, Q., and J. Revenaugh (2005), Ancient subduction, mantle eclogite, and the 300 km seismic discontinuity, *Geology*, *33*(1), 1–4.

Yuan, X., J. Ni, R. Kind, J. Mechie, and E. Sandvol (1997), Lithospheric and upper mantle structure of southern Tibet from a seismological passive source experiment, *J. Geophys. Res.*, *102*, 27,491–27,500.

Zhang, Y., Y. Wang, Y. Wu, C. Bina, Z. Jin, and S. Dong (2013), Phase transitions of harzburgite and buckled slab under eastern China, *Geochem. Geophys. Geosyst.*, *14*, 1182–1199, doi:10.1002/ggge.20069.